Intensity noise and modulation dynamics of an epitaxial mid-infrared interband cascade laser on silicon

H. Kim, P. Didier, S. Zaminga, D. Díaz-Thomas, A. Baranov, J. Rodriguez, E. Tournié, H. Knötig, B. Schwarz, L. Cerutti, et al.

APL Photonics

RESEARCH ARTICLE | OCTOBER 07 2024

Intensity noise and modulation dynamics of an epitaxial mid-infrared interband cascade laser on silicon

Special Collection: Mid-IR Photonics

H. Kim ✉ ; P. Didier ; S. Zaminga ; D. A. Díaz-Thomas ; A. N. Baranov ; J. B. Rodriguez ; E. Tournié ; H. Knötig ; B. Schwarz ; L. Cerutti ; O. Spitz ; F. Grillot

APL Photonics 9, 106103 (2024)
https://doi.org/10.1063/5.0214252

Intensity noise and modulation dynamics of an epitaxial mid-infrared interband cascade laser on silicon

Cite as: APL Photon. 9, 106103 (2024); doi: 10.1063/5.0214252
Submitted: 16 April 2024 • Accepted: 15 September 2024 •
Published Online: 7 October 2024

H. Kim,[1,a)] P. Didier,[1,2] S. Zaminga,[1] D. A. Díaz-Thomas,[3] A. N. Baranov,[3] J. B. Rodriguez,[3] E. Tournié,[3] H. Knötig,[4] B. Schwarz,[4] L. Cerutti,[3] O. Spitz,[5] and F. Grillot[1,6]

AFFILIATIONS

[1] LTCI Télécom Paris, Institut Polytechnique de Paris, 19 place Marguerite Perey, Palaiseau 91120, France
[2] mirSense, Campus Eiffel, Bâtiment E-RDC, 1 rue Jean Rostand, Orsay 91400, France
[3] Institut d'Electronique et des Systèmes, Université de Montpellier, CNRS UMR 5214, Montpellier 34000, France
[4] Institute for Solid State Electronics, TU Wien, Gußhausstraße 25-25a, 1040 Vienna, Austria
[5] The College of Optics and Photonics (CREOL), University of Central Florida, Orlando, Florida 32816, USA
[6] Center for High Technology Materials, University of New-Mexico, 1313 Goddard SE, Albuquerque, New Mexico 87106, USA

Note: This paper is part of the APL Photonics Special Topic on Mid-IR Photonics.
[a)] **Author to whom correspondence should be addressed:** hyunah.kim@telecom-paris.fr

ABSTRACT

Interband cascade lasers typically have significantly lower threshold current and power consumption than quantum cascade lasers. They can also have advantages regarding costs and compactness with the photonic integration onto silicon substrates by epitaxial growth. This research introduces a novel examination of the relative intensity noise and the modulation dynamics of a silicon-based Fabry–Perot interband cascade laser emitting at 3.5 μm. The investigation delves into crucial parameters, such as relaxation oscillation frequency, differential gain, gain compression, and K-factor. The resonance patterns identified in relative intensity noise curves can provide essential insights for the thorough characterization of high-defect mid-infrared semiconductor structures intended for high-speed applications. Moreover, this study demonstrates the feasibility of reaching 10 Gbit/s free-space transmission using a silicon-based interband cascade laser in conjunction with an interband cascade infrared photodetector.

I. INTRODUCTION

Mid-infrared technology is poised to enable several breakthroughs in domains as varied as gas spectroscopy,[1,2] free-space communications,[3,4] and optical countermeasures.[5] That said, large-scale deployment of mid-infrared systems is yet to come after almost 30 years of development in mid-infrared emitters based on semiconductor materials. Quantum cascade laser (QCL) was indeed first demonstrated in 1994,[6] while interband cascade laser (ICL) was first unveiled in 1995.[7] ICLs, with their structure relying on multiple quantum wells, differ from QCLs because of their working principle based on interband transition, which is associated with a longer recombination lifetime[8] (three orders of magnitude slower than QCLs'), as found in other diode lasers. Yet, ICLs retain the cascaded heterostructure technology of QCLs and combine it with type-II band alignment, which was proven efficient for mid-infrared emission.[9] This design preserves the advantages of cascade injection and the flexibility to tailor the emission wavelength through band-structure engineering.[10] The capability to manufacture high-quality mid-infrared lasers that are integrated on silicon can mark the beginning of a new era for this technology[11] as this means capability for large-scale production on the one hand[12] and compact, versatile systems on a chip on the other hand.[13] Moreover, it is relevant to note that recent studies about lab-on-a-chip mid-infrared spectroscopy are already weighing in photonics integrated circuits (PICs) at mid-infrared wavelength.[14–16] Despite the fact that the

first mid-infrared semiconductor lasers on silicon were QCLs,[17,18] ICLs are particularly interesting for integration on silicon because of their low-power consumption.[19,20] Furthermore, ICLs have proven to be resistant to defects, such as outstanding immunity to threading dislocations.[21,22] Therefore, it is no surprise that the topic of ICLs on silicon has attracted increased interest during the past years[23,24] as an integral part of the development of various fundamental mid-infrared photonic components.[25] So far, manufacturing efforts have shown that ICLs directly grown on silicon can exhibit performances similar to their counterparts grown on native GaSb.[22,23] Yet, most of these studies are limited to the description of material properties of ICL grown on silicon, without any characterization of their high-speed electrical properties or demonstration of real-field applications. Despite the need for thick GaSb buffer layers to isolate the optical mode from the underlying silicon during silicon integration, one potential solution is to employ monolithically integrated semiconductor lasers with a butt-coupling waveguide.[26–28]

In parallel, ICLs grown on GaSb have already shown impressive capabilities in terms of portable spectroscopy, including their use in the methane detector aboard the NASA Curiosity rover,[29] or in terms of electrical bandwidth for high-speed applications. A few years ago, an article investigating the relative intensity noise (RIN)[30] of GaSb-based ICL disclosed a relaxation oscillation frequency in the GHz range, thereby indicating a potential bandwidth for direct electrical modulation of around 2.5 GHz.[31] This confirmed the results observed in early studies with cryogenic ICLs.[32] More recently, a comprehensive interband cascade system, incorporating a Fabry–Perot (FP) ICL and an interband cascade infrared photodetector (ICIP),[33,34] achieved data rates of up to 12 Gbit/s using on–off keying (OOK) and 14 Gbit/s with a four-level pulse amplitude modulation (PAM) scheme.[35] This result outperformed the early transmission rates[36] and the recent efforts with external modulators[37,38] by several orders of magnitude, remaining so far the fastest free-space communication in the 3–5 μm transparency windows of the atmosphere[39,40] with direct modulation of semiconductor lasers. Last but not least, in addition to conventional distributed feedback (DFB) and external-cavity strategies,[41] new techniques are being currently developed to design single-mode ICLs using slotted waveguides,[42] which will pave the way for multiplexing of mid-infrared beams, both for spectroscopy and high-speed applications.

This work explores the RIN properties and the modulation dynamics of an epitaxial FP ICL, whose emitting wavelength is around 3.5 μm, directly grown on a silicon substrate. The study of RIN allows extraction of intrinsic laser parameters, such as differential gain, gain compression, and K-factor,[43] focusing on the capabilities for high-speed applications based on direct modulation of this mid-infrared laser on silicon. At high bias current, the relaxation oscillation is found in the range of a few hundreds of MHz, resulting in a theoretical modulation bandwidth of 1 GHz, which is aligned with the measured bandwidth. These investigations lead to the realization of a proof-of-concept multi-Gbit/s transmission with direct modulation of an epitaxial silicon-based ICL coupled with an ICIP detector. Overall, this work is a milestone in the realization of PIC in the 3–5 μm optical domain that opens the way for energy-efficient high-speed applications with epitaxially grown ICLs.

II. ICL ON SILICON

The ICL on silicon is presented in this work with the structure described in Fig. 1. This ICL was designed and fabricated

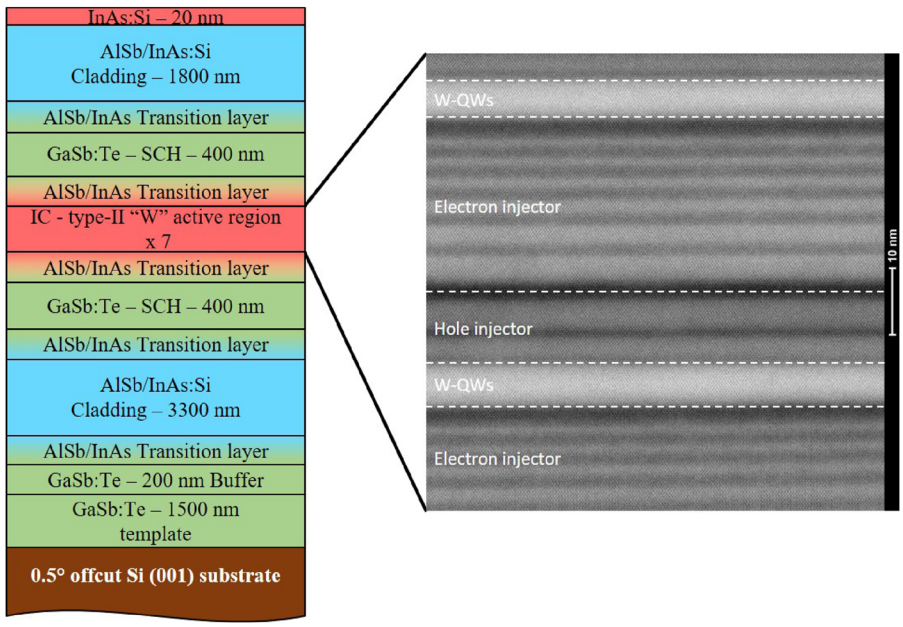

FIG. 1. Schematic of the ICL structure grown on a silicon substrate with the cross-sectional TEM image of 1.5 stages of the active region.

by the Université de Montpellier using solid-state molecular beam epitaxy (MBE) on a 2-in. (001) silicon substrate, oriented with a 0.5° offcut to the [110] direction. Following the growth of a 200 nm thick GaSb buffer using the procedure outlined in Ref. 44, the laser structure was meticulously grown.[22] Comprising seven active stages designed for emission at 3.5 μm,[45] these active stages were interposed between two 400 nm-thick separate GaSb confinement layers with low Te doping. The top and bottom cladding layers, constructed from AlSb/InAs superlattices, have respective thicknesses of 1.8 and 3.3 μm.

The structural refinement continued with the processing of the structure into 10 μm-wide ridges FP lasers, employing standard photolithography and chlorine-based inductively coupled plasma reactive ion etching (ICP-RIE). Electrical insulation was achieved using AZ1518 photoresist, and Ti/Au served as the contact metal for both the top and bottom contacts. The laser cavities were formed by cleaving the chips without additional optical treatment applied to the facets. For packaging, the devices were soldered epi-side up using indium on a specialized platform that facilitated a direct connection between the SMA core contact and the laser ridge.[31]

Subsequently, the electro-optical characterization of this ICL on silicon was performed, as illustrated in Fig. 2. First, the voltage and optical power of the ICL are measured under continuous wave pumping at room temperature. As depicted in Fig. 2(a), the ICL has a threshold current of 59 mA at a temperature of 293 K and a maximum power of 11 mW with a bias current of 186 mA and a voltage of 6.1 V. The optical spectrum of the ICL is also displayed in this figure, proving that this ICL has a lasing wavelength of around 3.5 μm. In Fig. 2(b), the frequency response of the ICL is shown in order to evaluate the bandwidth by using a 40 GHz bandwidth vector network analyzer (VNA, Rohde & Schwarz-ZVK) and the 1.5 GHz bandwidth ICIP detector. As a result, this ICL shows a 3-dB bandwidth of 1 GHz, with a flat response for lower frequencies. Details about the experimental setup allowing the characterization of the bandwidth are given in Sec. IV.

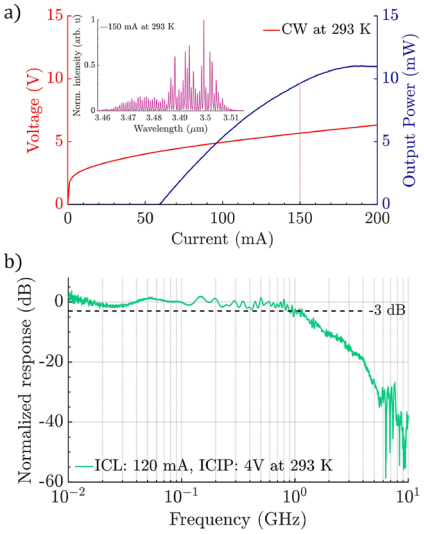

FIG. 2. (a) Light–intensity–voltage (LIV) curve of the ICL whose working wavelength is around 3.5 μm under continuous wave pumping at room temperature. The inset is the optical spectrum showing the wavelength of emission with a bias current of 150 mA at 293 K. (b) Normalized frequency response of the ICL when biased at 120 mA and with the ICIP biased at 4 V under 293 K, measured with a VNA.

III. RELATIVE INTENSITY NOISE

The RIN corresponds to the light intensity fluctuations relative to the average intensity. The RIN is thus expressed as a ratio of the optical output power noise to its average power from the emitting facet. If the semiconductor laser has a high level of RIN, there will be a deterioration in performance for high-speed applications due to the reduced signal-to-noise ratio and increased error rate.[30] The RIN investigation allows deriving several intrinsic parameters of the laser and provides information in order to improve the quality of high-speed communication with direct modulation of the laser.

The experimental setup to perform the RIN measurement is shown in Fig. 3, and this configuration is similar to that used in the prior investigation.[31] The photodetector converts the optical signal sent by the ICL, biased with a low-noise current source, to the electrical signal, whose AC component is amplified and directed to the electrical spectrum analyzer (ESA, FSU Rohde&Schwarz). We can then derive the RIN with the acquired data from the ESA by calculating as follows:[30]

$$RIN(f) = \frac{N_{ph}(f)}{GBRI_{ph}^2} - \frac{2e}{\langle I_{ph}\rangle}, \tag{1}$$

with $N_{ph}(f)$ being the intrinsic laser noise [obtained by subtracting thermal noise $N_{therm}(f)$ from the total noise $N_{total}(f)$ measured by the ESA], G being the gain coefficient of the amplifier, B being the resolution bandwidth of the ESA, R being the resistance of the photodetector, e being the electric charge of an electron, and I_{ph} being the photocurrent of the photodetector.

Figure 4 illustrates the RIN when the experiment is carried out with a Mercury–Cadmium–Telluride (MCT, Vigo Photonics UHSM-I-10.6) photodetector when applying various bias currents to the ICL, from 2.19 $\times I_{th}$ to 2.81 $\times I_{th}$. Since the MCT has a narrow bandwidth of 700 MHz, the shot noise level is impossible to extract clearly within the bandwidth. It displays two distinct behaviors with respect to the change in relaxation oscillation frequency with the

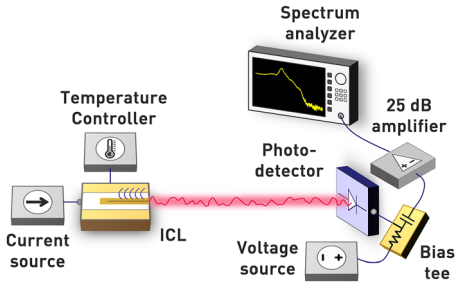

FIG. 3. Experimental setup for extracting the RIN. The ICL is kept at room temperature and the photodetector is placed roughly 1 m away from the emitting facet. The electrical signal from this photodetector is amplified and fed to an electrical spectrum analyzer.

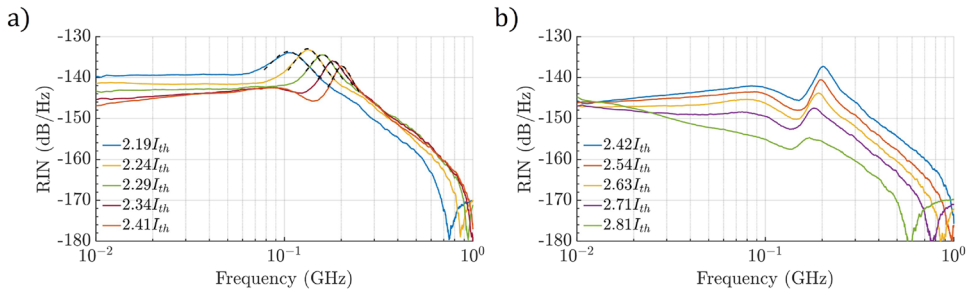

FIG. 4. RIN of the ICL at 293 K measured for several bias currents from 2.19 $\times I_{th}$ to 2.81 $\times I_{th}$, showing two opposite behaviors. (a) From 2.19 $\times I_{th}$ to 2.41 $\times I_{th}$, the relaxation oscillation frequency increases as we increase the bias current. (b) Conversely, the relaxation oscillation frequency decreases with the increasing bias current from 2.42 $\times I_{th}$ to 2.81 $\times I_{th}$.

bias current. First, the RIN curves when the ICL is biased from 2.19 $\times I_{th}$ to 2.41 $\times I_{th}$ are described in Fig. 4(a). Within the low-frequency range of ~10–60 MHz, the RIN level is kept constant between −140 and −150 dB/Hz for a given bias current and decreases when the bias current increases. Within the 100–200 MHz frequency range, the relaxation oscillation frequency is observed, increasing with the bias current. On the other hand, in Fig. 4(b), when the ICL is biased from 2.42 $\times I_{th}$ to 2.81 $\times I_{th}$, the RIN level is observed at around −146 dB/Hz at 10 MHz. At the lower frequency range, the RIN level decreases with the bias current, similarly to what has been seen in Fig. 4(a). However, higher bias currents exhibit a relaxation oscillation frequency ranging from about 150–200 MHz, which decreases with an increase in bias current. The decrease in the relaxation oscillation frequency likely stems from the gain saturation observed in the LIV measurements above 150 mA. This gain saturation is due to a significantly large gain compression factor, which will be discussed in further detail hereinafter. Even though the relaxation oscillation frequency shows a different behavior starting from a bias current of 2.42 $\times I_{th}$, the RIN amplitude always decreases with the bias current, meaning that the laser becomes more damped with increasing photon density, as expected from the theory.[30]

Between the two regimes that are shown in Fig. 4, we focus on the configuration in Fig. 4(a) where the relaxation oscillation frequency increases when increasing the bias current, as expected, to explore the modulation dynamics parameters. The black dashed lines in Fig. 4(a) represent the resonance fitting that allows deriving intrinsic laser parameters, including the damping factor and K-factor. Retrieving such parameters requires examining small-signal frequency responses near the relaxation oscillation using rate equations. The relevant equations and parameters, such as the ICL's characteristics, are reused from the previous work,[31] except for the cavity length of 2 mm, internal loss of 3.95 cm^{-1}, photon lifetime of 12.1 ps, injection efficiency of 2.52 (0.36 per stage), transparent carrier number of 2.8×10^8, and the differential gain, which is detailed hereafter.

A. Intrinsic parameters of the ICL

The differential gain is determined by the derivative dg/dN, which indicates the rate of change of gain (g) with the carrier density (N). A high differential gain is thus effective for enhancing the high-speed abilities of the laser. Here, the differential gain is retrieved by

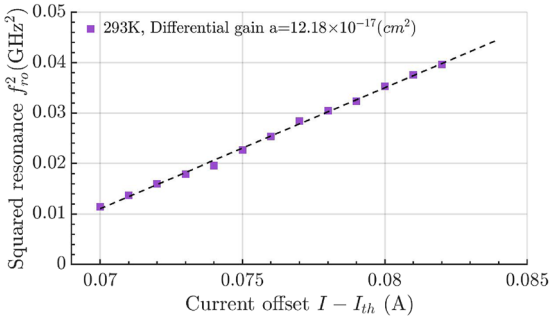

FIG. 5. Squared resonance frequency with respect to the current offset $I - I_{th}$. The dashed line indicates the linear fitting and yields the differential gain value.

plotting the squared resonance frequency as a function of the current offset,[30] as described in Fig. 5. By applying the equation used for the linear fitting in this plot, the differential gain is estimated as 12.18×10^{-17} cm^2. Compared to the previous study, this is two times higher than that of the ICL on GaSb emitting at 4.1 μm, which is 6×10^{-17} cm^2.[31] Since the laser structures are fundamentally the same, except for the quantum well thickness, which is adjusted to achieve the desired wavelength, and for the electron injectors, which ensure proper level alignment at the appropriate bias voltage, we believe that the increase in differential gain can largely be attributed to a greater overlap of the wavefunctions at shorter wavelengths. In addition, a large value of the differential gain can result in a smaller linewidth enhancement factor and, subsequently, a higher reflection immunity as already reported in epitaxial quantum dot (QD) lasers on silicon.[46]

Additionally, the damping factor γ is investigated from the curve fitting in Fig. 4(a). The damping factor is then plotted for various squared resonance frequencies, as depicted in Fig. 6. Here, another parameter that can be considered a relevant indication for high-speed applications, the K-factor, can be retrieved by linear fitting in this plot. The K-factor may allow estimating the maximum modulation bandwidth with the following formula: $2\sqrt{2}\pi/K$.[47] As a result, the K-factor is calculated as 9.57 ns, which yields a maximum modulation bandwidth of 0.93 GHz. As one can note from Fig. 2(b), this 0.93 GHz bandwidth is close to our measured bandwidth.

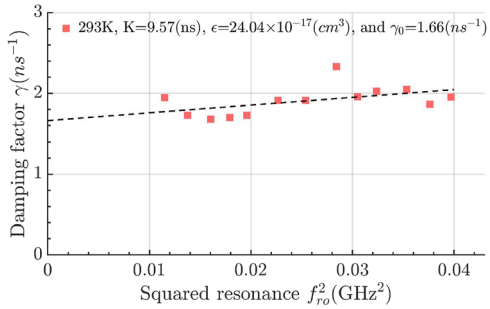

FIG. 6. Variation of the damping factor as a function of squared resonance frequency. The dashed line indicates the linear fitting, which is of interest for the derivation of parameters such as the K-factor and the gain compression factor.

Other parameters, such as the gain compression factor ϵ and the damping offset γ_0, are also derived from this plot. The gain compression indicates the reduction of gain or amplification when the input signal increases. Thus, optimization of high-speed communication requires the analysis of this parameter, which provides the non-linearity of the system and may affect the transmission performances. The compression factor, calculated by the equation that links the K-factor, the gain compression, the differential gain, and the photon lifetime,[31] is estimated as 24.04×10^{-17} cm^3, which is more than five times as large as that of our previous work on ICL on GaSb, with the value 4.7×10^{-17} cm^3.[31] This high value of gain compression, comparable to that observed in QD lasers, contributes to the decrease in the ICL's relaxation oscillation frequency. This issue can be resolved by increasing the maximum gain of the active region to prevent gain saturation. Gain compression is essentially due to spectral hole burning and carrier heating. For ICLs on Si, we have not yet figured out why a stronger gain compression occurs. Nevertheless, one can imagine that when the optical mode intensity is high, as in the case of very strong signals, it is more affected by scattering on the defects or by absorption, which somewhat limits the linearity range of the gain. However, further investigation into the origins of this high gain compression is necessary. Additionally, it is important to emphasize that the carrier transport time across the heterostructure can alter the relaxation oscillation frequency and the modulation dynamics by introducing a parasitic term. Furthermore, the damping offset of 1.66 ns^{-1} allows estimating the differential carrier lifetime of 0.6 ns. This value fundamentally depends on the injected carrier density, meaning that it can vary and increase due to increased nonlinearities that occur at higher bias.

IV. HIGH SPEED TRANSMISSION WITH THE RF-OPTIMIZED ICL ON SILICON

After the characterization of the intrinsic parameters, the evaluation of the capability of the ICL on silicon for free-space transmission is performed. The evaluation of the full setup's bandwidth, consisting of amplifiers, laser, and detector, utilized a VNA with 40 GHz bandwidth. The VNA, comprising an electrical source signal and receiver, determines the input–output relationship between system ports based on the source signal frequency. In this experiment, the VNA's source signal was connected to the AC port of the laser's bias tee, while the receiver was linked to the 25-dB amplified response signal of the ICIP. This configuration provided the amplitude response of the system as a function of the modulating frequency. The resulting response remained relatively flat until reaching the cut-off frequency, as illustrated in Fig. 2(b). It is noteworthy that the system's speed is constrained by the laser even at high bias current that should provide the largest modulation bandwidth.[35] The 3-dB bandwidth of the ICIP has been previously assessed and found to be around 1.5 GHz. Further details about the ICIP detector can be found in Ref. 35.

With the configuration described in Fig. 7, the system's capability to transmit information at various data rates and across various modulation schemes is assessed. In this evaluation, a 2^{15}-bit long pseudo-random binary sequence (PRBS) is implemented for two different formats (OOK, PAM-4). For each transmission, time traces consisting of ten million points are recorded at a sampling rate of 50 GS/s, which is the maximum sampling rate of the oscilloscope (Tektronix, DPO72004B). A root-raised-cosine (RRC) pulse-shaping filter is used with several roll-off factors (ρ) to minimize the spectral occupation of the transmitted signal.[35] The roll-off factor minimizing the bit error rate (BER) is found to be around 0.3. At the receiver side, a matched filter, corresponding to an RRC filter with the same roll-off factor, is applied. The signal undergoes equalization through a fractionally spaced feed-forward equalization (FFE) at a rate of four samples per symbol. The FFE algorithm learns the coefficients of the channel equalizer using a least-mean-square gradient descent approach with a convergence parameter (μ) to control the learning step's speed and accuracy. The number of filter coefficients, denoted as n_{tap}, is also necessary to cover the channel memory adequately. Once the algorithm converges to achieve an error below a given threshold, the estimated equalizer is applied to the received signal to eliminate the inter-symbol-interference (ISI).

The eye diagrams in Fig. 8 are plotted to visualize the system's ability to distinguish between different bit levels. Distortions in the eye can indicate non-linearity or systematic errors in the transmitted signal. Compression between different bit levels or an ill-defined eye level also provides insights. In the example shown here, the eyes do

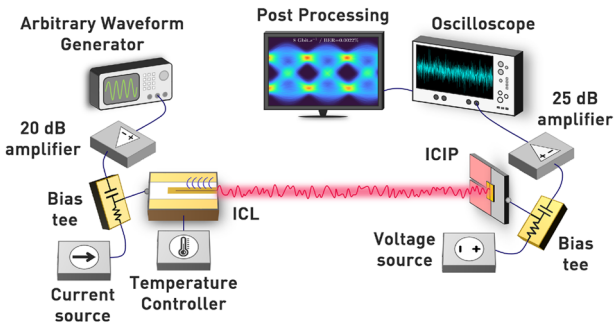

FIG. 7. Experimental setup for high-speed transmission in the mid-infrared domain using interband cascade devices. An ICL emitting at a wavelength of around 3.5 μm generates ~10 mW of optical power. The laser is subject to direct modulation through a 20-dB amplified signal generated by an arbitrary waveform generator (AWG). The modulated optical wave is then detected by an ICIP detector, which converts it into an electrical signal. This electrical signal is then directed to a high-speed oscilloscope for recording and analysis.

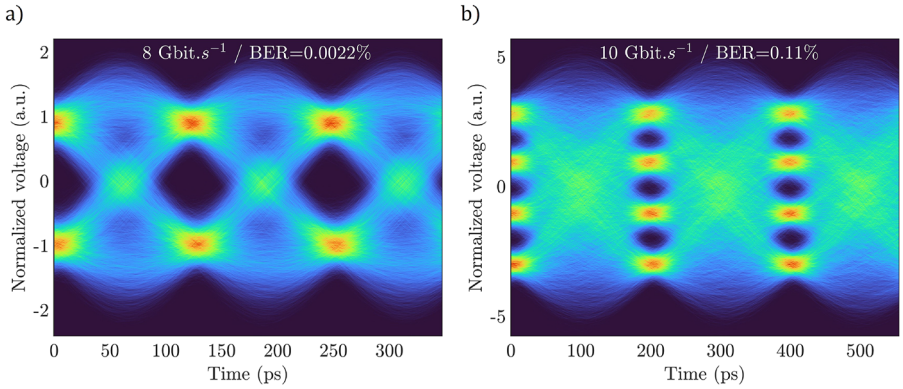

FIG. 8. Eye diagrams of the transmission following a free-space propagation of ~2 m for two distinct modulation formats. An eye diagram depicts the superimposition of the recorded signal at a fixed time interval corresponding to an integer multiple of the bit time-length. This tool enables a qualitative assessment of transmission performance, with an open eye indicating a low error rate by showcasing the ability to distinguish between different modulation levels. (a) OOK format at 8 Gbit/s, demonstrating an error rate of 0.0022%. (b) PAM-4 format at 10 Gbit/s with an error rate of 0.11%. In both instances, there exists a specific set of parameters where equalization significantly enhances the quality of the transmission.

not show main distortion or compression, underscoring the quality of our free-space transmission. In order to achieve such a result corresponding to the lowest BER (and that is not attainable without processing because this system has 1 GHz bandwidth), we had to optimize equalization parameters.

For two-level modulation (OOK), an optimal μ value of around 10^{-3} and n_{tap} above 11 were necessary to meet a tabulated threshold BER. Notably, the equalization process significantly improved the transmission quality only for well-chosen parameters. Through optimization, the OOK transmission succeeded in reaching bit rates of 8 Gbit/s with a BER below 0.4% and 10 Gbit/s with a BER under 4%. For the 4-level format (PAM-4), the optimal μ factor was about 10^{-4}, and n_{tap} above 391 was selected. The transmission could achieve 10 Gbit/s with a BER below 0.4% and 12 Gbit/s with a BER under 4%. The results meeting the BER <4% criterion can be found in Appendix C. It is relevant to note that the optimal value of the convergence parameter μ tends to be lower (which corresponds to a more accurate but slower estimation during real-time signal processing) when considering multi-level modulation formats. Additionally, the aforementioned BER levels (0.4% and 4%) align with forward error correction (FEC) coding, which is used to correct bit errors and is required to obtain an error-free transmission.

V. CONCLUSION

This study presented an achievement in the development and application of a mid-infrared ICL integrated onto a silicon substrate and explored its intrinsic properties. The first phase of the study investigated the relative intensity noise and high-speed parameters of the ICL emitting at 3.5 μm. Our results revealed the existence of relaxation oscillation frequency in the hundreds of MHz, which is crucial for understanding and, in the future, enhancing the direct modulation capabilities. The comprehensive analysis of parameters such as differential gain, K-factor, gain compression, and differential carrier lifetime aligns well with reported values in interband quantum well lasers. During the second phase, taking advantage of the results on relative intensity noise and high-speed capabilities, we effectively demonstrated the viability of a comprehensive interband cascade system within one of the transparency windows in the atmosphere. This endeavor resulted in achieving remarkable data rates, ranging from 8 to 10 Gbit/s, utilizing OOK and PAM-4 modulation formats. The utilization of cascaded interband devices implemented on silicon is of utter interest for high-speed applications in the mid-infrared, offering a significant reduction in power consumption and ease of implementation on photonics integrated circuits compared to QCLs. Overall, these findings position ICLs as promising candidates for versatile, lightweight, and cost-effective multi-Gbit/s transmission systems in the mid-infrared domain. The highlighted efforts in achieving high data rates, coupled with the inherent properties of ICLs, open avenues for applications with already existing very-high-speed detectors in the 3–5 μm window, such as quantum well-infrared photodetectors (QWIPs) and quantum cascade detectors (QCDs), among others.[48–50] Future experiments will explore single-mode ICLs as well as noise reduction strategies, potentially boosting applications that demand ultra-low laser noise, including precision measurement, metrology, spectroscopy, and continuous-variable quantum systems.[51] Last but not least, pump–probe experiments could also provide relevant information about the carrier dynamics and the different contributions to the nonlinear gain. Despite these accomplishments, ongoing work focuses on enhancing the speed of both the laser and the detector as those two key components are not currently limited by fundamental physical properties that would hinder larger bandwidths.

ACKNOWLEDGMENTS

This work was supported by the French Defense Agency (DGA), the French ANR program (Grant Nos. ANR-17-ASMA0006 and ANR-11-EQPX-0016), the European Office of Aerospace Research and Development (Grant No. FA9550-18-1-7001), and the European Research Council (ERC) under the European Union's Horizon 2020 research and innovation program (Grant Agreement

No. 853014). The ICIP used in this experiment was grown and provided by Nanoplus.

AUTHOR DECLARATIONS

Conflict of Interest

The authors have no conflicts to disclose.

Author Contributions

H. Kim: Conceptualization (equal); Data curation (lead); Formal analysis (lead); Software (lead); Writing – original draft (equal); Writing – review & editing (equal). **P. Didier**: Software (supporting); Writing – original draft (equal). **S. Zaminga**: Investigation (supporting). **D. A. Díaz-Thomas**: Resources (supporting). **A. N. Baranov**: Resources (supporting). **J. B. Rodriguez**: Resources (supporting). **E. Tournié**: Resources (supporting). **H. Knötig**: Resources (supporting). **B. Schwarz**: Resources (supporting); Writing – review & editing (supporting). **L. Cerutti**: Resources (supporting); Writing – review & editing (supporting). **O. Spitz**: Conceptualization (equal); Formal analysis (supporting); Supervision (equal); Writing – original draft (equal); Writing – review & editing (equal). **F. Grillot**: Conceptualization (equal); Project administration (equal); Supervision (equal); Writing – review & editing (equal).

DATA AVAILABILITY

The data that support the findings of this study are available from the corresponding author upon reasonable request.

APPENDIX A: RIN WITH ICIP

RIN of the ICL on silicon is analyzed with the ICIP detector having a bandwidth of around 1.5 GHz, which is larger than the MCT bandwidth. As seen in Fig. 9, at the lower frequency range, unlike with the MCT detector, the RIN level does not show much dependence on the bias current, maintaining a value of −130 dB/Hz. Since the ICIP detector has a smaller active area compared to the MCT detector (see Table I), the spatial components of the beam are partially clipped by the ICIP, which possibly leads to spatial mode partition when the ICL becomes spatially multimode, for large bias currents.[52] This can explain why the measurements carried out with the ICIP detector showed higher RIN levels.

The relaxation oscillation frequencies are observed at between 100 and 200 MHz, increasing with the bias current in Fig. 9(a) and decreasing when increasing the bias current in Fig. 9(b). The two opposite regimes regarding the resonance frequency are identical to those observed with the MCT detector. Also of interest is the observable shot noise level, which is around −162 dB/Hz, due to the ICIP detector having a larger bandwidth of 1.5 GHz.

The same parameter extraction was performed from the RIN measured with the ICIP detector. One can find the differential gain from the curve fitting in Fig. 10, giving $a = 12.85 \times 10^{-17}$ cm^2, which is compatible with the differential gain value obtained with the MCT.

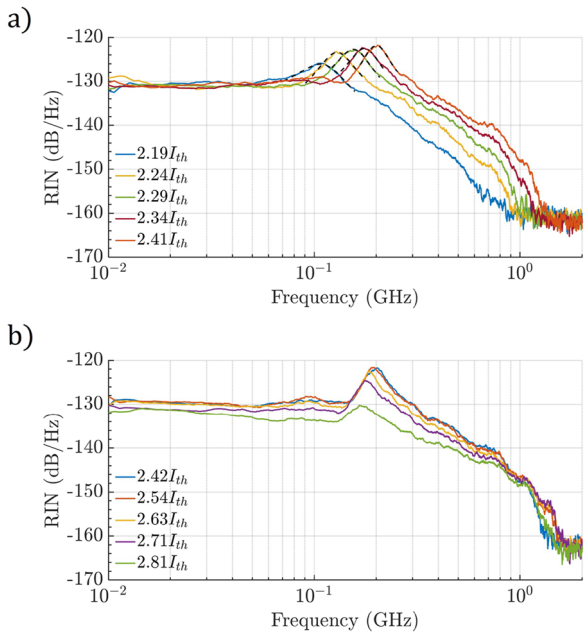

FIG. 9. RIN of the ICL at 293 K for several bias currents from 2.19 $\times I_{th}$ to 2.81 $\times I_{th}$. These experimental data were retrieved with the ICIP detector, but similarly to what has been shown with the MCT, (a) from 2.19 $\times I_{th}$ to 2.41 $\times I_{th}$, the relaxation oscillation frequency increases as we increase the bias current. (b) Conversely, the relaxation oscillation frequency decreases with the increasing bias current from 2.42 $\times I_{th}$ to 2.81 $\times I_{th}$.

Subsequently, a K-factor value of 8.8 ns is derived by plotting the damping factor as a function of the squared resonance frequency, as depicted in Fig. 11. As a result, the maximum modulation bandwidth is found to be 1 GHz, while the gain compression coefficient is 23.22×10^{-17} cm^3. Moreover, the damping offset of 1.91 ns^{-1} gives an estimated differential carrier lifetime of 0.52 ns.

APPENDIX B: COMPARISON OF PHOTODETECTORS

Table I compares the main properties of two photodetectors, MCT and ICIP, used in this RIN study. Although the ICIP detector was useful in showing the shot noise level, thanks to its larger bandwidth of around 1.5 GHz, the MCT detector showed around

TABLE I. Comparison of MCT and ICIP used for the RIN measurement in this study.

	MCT[53]	ICIP[35]
Power consumption	<1 W	<1 W
Operating temperature	Peltier cooled	RT (293 K)
Cut-off wavelength (μm)	2.5–12	2–4.5
Responsivity (mA/W)	≥500	130
Detectivity (Jones)	$\geq 1.0 \times 10^9$	$\approx 4.42 \times 10^8$
Active area size (μm^2)	10^6 (square)	$\approx 1.77 \times 10^4$ (circle)
Bandwidth (GHz)	0.7	1.5
Polarization selection rules	No	No

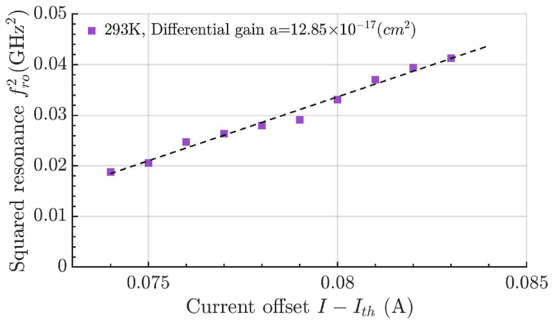

FIG. 10. Squared resonance frequency with respect to the current offset $I - I_{th}$. The dashed line indicates the linear fitting and yields the differential gain value.

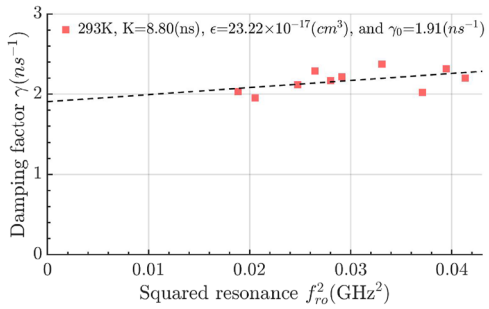

FIG. 11. Variation of the damping factor as a function of squared resonance frequency. The dashed line indicates the linear fitting and is of interest for the derivation of parameters such as the K-factor and the gain compression factor.

10 dB/Hz lower RIN level, potentially because of spatial mode partitioning, and gave better insights for intrinsic parameters extraction due to its higher responsivity and detectivity.

APPENDIX C: TRANSMISSION RESULTS

As mentioned in the main text, eye diagrams of the transmission investigation for higher bit rates are presented in Fig. 12 for the OOK format and in Fig. 13 for the PAM-4 format. They succeeded

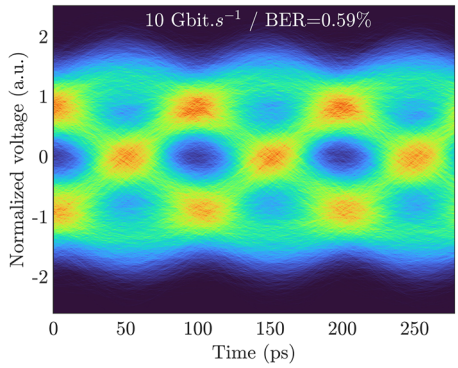

FIG. 12. Eye diagram of the transmission following a free-space propagation of ~2 m for an OOK format at 10 Gbit/s, demonstrating an error rate of 0.59%.

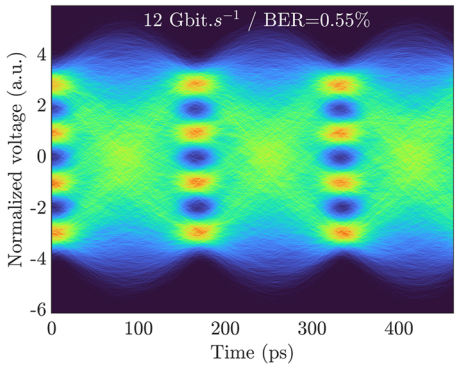

FIG. 13. Eye diagrams of the transmission following a free-space propagation of ~2 m for a PAM-4 format at 12 Gbit/s, demonstrating an error rate of 0.55%.

in reaching up to 10 Gbit/s with an error rate of 0.59% and 12 Gbit/s with an error rate of 0.55%, respectively.

REFERENCES

[1]J. H. Northern, S. O'Hagan, B. Fletcher, B. Gras, P. Ewart, C. S. Kim, M. Kim, C. D. Merritt, W. W. Bewley, C. L. Canedy *et al.*, "Mid-infrared multi-mode absorption spectroscopy using interband cascade lasers for multi-species sensing," Opt. Lett. **40**, 4186–4189 (2015).
[2]N. M. Davis, D. Francis, J. Hodgkinson, and R. P. Tatam, "Compact methane sensor using an integrating sphere and interband cascade laser at 3313 nm," Sens. Actuators, B **389**, 133866 (2023).
[3]X. Pang, R. Schatz, M. Joharifar, A. Udalcovs, V. Bobrovs, L. Zhang, X. Yu, Y.-T. Sun, G. Maisons, M. Carras *et al.*, "Direct modulation and free-space transmissions of up to 6 Gbps multilevel signals with a 4.65-μm quantum cascade laser at room temperature," J. Lightwave Technol. **40**, 2370–2377 (2022).
[4]K. Zou, K. Pang, H. Song, J. Fan, Z. Zhao, H. Song, R. Zhang, H. Zhou, A. Minoofar, C. Liu *et al.*, "High-capacity free-space optical communications using wavelength- and mode-division-multiplexing in the mid-infrared region," Nat. Commun. **13**, 7662 (2022).
[5]S. G. Lorenzo, C. You, C. H. Granier, G. Veronis, and J. P. Dowling, "Optimized mid-infrared thermal emitters for applications in aircraft countermeasures," AIP Adv. **7**, 125112 (2017).
[6]J. Faist, F. Capasso, D. L. Sivco, C. Sirtori, A. L. Hutchinson, and A. Y. Cho, "Quantum cascade laser," Science **264**, 553–556 (1994).
[7]R. Q. Yang, "Infrared laser based on intersubband transitions in quantum wells," Superlattices Microstruct. **17**, 77–83 (1995).
[8]W. Bewley, J. Lindle, C. Kim, M. Kim, C. Canedy, I. Vurgaftman, and J. Meyer, "Lifetimes and Auger coefficients in type-II W interband cascade lasers," Appl. Phys. Lett. **93**, 041118 (2008).
[9]J. R. Meyer, C. A. Hoffman, F. J. Bartoli, and L. R. Ram-Mohan, "Type-II quantum-well lasers for the mid-wavelength infrared," Appl. Phys. Lett. **67**, 757–759 (1995).
[10]I. Vurgaftman, R. Weih, M. Kamp, J. Meyer, C. Canedy, C. Kim, M. Kim, W. Bewley, C. Merritt, J. Abell, and S. Höfling, "Interband cascade lasers," J. Phys. D: Appl. Phys. **48**, 123001 (2015).
[11]R. Soref, "Mid-infrared photonics in silicon and germanium," Nat. Photonics **4**, 495–497 (2010).
[12]D. Liang and J. E. Bowers, "Recent progress in lasers on silicon," Nat. Photonics **4**, 511–517 (2010).
[13]T. Hu, B. Dong, X. Luo, T.-Y. Liow, J. Song, C. Lee, and G.-Q. Lo, "Silicon photonic platforms for mid-infrared applications [Invited]," Photonics Res. **5**, 417–430 (2017).

[14]H. Lotfi, L. Li, S. Shazzad Rassel, R. Q. Yang, C. J. Corrége, M. B. Johnson, P. R. Larson, and J. A. Gupta, "Monolithically integrated mid-IR interband cascade laser and photodetector operating at room temperature," Appl. Phys. Lett. **109**, 151111 (2016).
[15]A. Vasiliev, A. Malik, M. Muneeb, B. Kuyken, R. Baets, and G. Roelkens, "On-chip mid-infrared photothermal spectroscopy using suspended silicon-on-insulator microring resonators," ACS Sensors **1**, 1301–1307 (2016).
[16]B. Hinkov, F. Pilat, L. Lux, P. L. Souza, M. David, A. Schwaighofer, D. Ristanić, B. Schwarz, H. Detz, A. M. Andrews *et al.*, "A mid-infrared lab-on-a-chip for dynamic reaction monitoring," Nat. Commun. **13**, 4753 (2022).
[17]Z. Loghmari, J.-B. Rodriguez, A. Baranov, M. Rio-Calvo, L. Cerutti, A. Meguekam, M. Bahriz, R. Teissier, and E. Tournié, "InAs-based quantum cascade lasers grown on on-axis (001) silicon substrate," APL Photonics **5**, 041302 (2020).
[18]H. Nguyen-Van, A. N. Baranov, Z. Loghmari, L. Cerutti, J.-B. Rodriguez, J. Tournet, G. Narcy, G. Boissier, G. Patriarche, M. Bahriz *et al.*, "Quantum cascade lasers grown on silicon," Sci. Rep. **8**, 7206 (2018).
[19]I. Vurgaftman, W. Bewley, C. Canedy, C. Kim, M. Kim, C. Merritt, J. Abell, J. Lindle, and J. Meyer, "Rebalancing of internally generated carriers for mid-infrared interband cascade lasers with very low power consumption," Nat. Commun. **2**, 585 (2011).
[20]I. Vurgaftman, W. W. Bewley, C. L. Canedy, C. S. Kim, M. Kim, C. D. Merritt, J. Abell, and J. R. Meyer, "Interband cascade lasers with low threshold powers and high output powers," IEEE J. Sel. Top. Quantum Electron. **19**, 1200210 (2013).
[21]M. Niehle, J.-B. Rodriguez, L. Cerutti, E. Tournié, and A. Trampert, "On the origin of threading dislocations during epitaxial growth of III-Sb on Si(001): A comprehensive transmission electron tomography and microscopy study," Acta Mater. **143**, 121–129 (2018).
[22]L. Cerutti, D. A. Díaz Thomas, J.-B. Rodriguez, M. Rio Calvo, G. Patriarche, A. N. Baranov, and E. Tournié, "Quantum well interband semiconductor lasers highly tolerant to dislocations," Optica **8**, 1397–1402 (2021).
[23]M. Rio Calvo, L. Monge Bartolomé, M. Bahriz, G. Boissier, L. Cerutti, J.-B. Rodriguez, and E. Tournié, "Mid-infrared laser diodes epitaxially grown on on-axis (001) silicon," Optica **7**, 263–266 (2020).
[24]E. Tournié, L. Monge Bartolome, M. Rio Calvo, Z. Loghmari, D. A. Díaz-Thomas, R. Teissier, A. N. Baranov, L. Cerutti, and J.-B. Rodriguez, "Mid-infrared III–V semiconductor lasers epitaxially grown on Si substrates," Light: Sci. Appl. **11**, 165 (2022).
[25]Y. Zou, S. Chakravarty, C.-J. Chung, X. Xu, and R. T. Chen, "Mid-infrared silicon photonic waveguides and devices [Invited]," Photonics Res. **6**, 254–276 (2018).
[26]A. Remis, L. Monge-Bartolome, M. Paparella, A. Gilbert, G. Boissier, M. Grande, A. Blake, L. O'faolain, L. Cerutti, J.-B. Rodriguez, and E. Tournié, "Unlocking the monolithic integration scenario: Optical coupling between GaSb diode lasers epitaxially grown on patterned Si substrates and passive SiN waveguides," Light: Sci. Appl. **12**, 150 (2023).
[27]K. Feng, C. Shang, E. Hughes, A. Clark, R. Koscica, P. Ludewig, D. Harame, and J. Bowers, "Quantum dot lasers directly grown on 300 mm Si wafers: Planar and in-pocket," Photonics **10**, 534 (2023).
[28]W.-Q. Wei, A. He, B. Yang, Z.-H. Wang, J.-Z. Huang, D. Han, M. Ming, X. Guo, Y. Su, J.-J. Zhang, and T. Wang, "Monolithic integration of embedded III-V lasers on SOI," Light: Sci. Appl. **12**, 84 (2023).
[29]C. R. Webster, P. R. Mahaffy, S. K. Atreya, J. E. Moores, G. J. Flesch, C. Malespin, C. P. McKay, G. Martinez, C. L. Smith, J. Martin-Torres *et al.*, "Background levels of methane in Mars' atmosphere show strong seasonal variations," Science **360**, 1093–1096 (2018).
[30]L. A. Coldren, S. W. Corzine, and M. L. Mashanovitch, *Diode Lasers and Photonic Integrated Circuits* (John Wiley & Sons, 2012).
[31]P. Didier, O. Spitz, L. Cerutti, D. Diaz-Thomas, A. Baranov, M. Carras, and F. Grillot, "Relative intensity noise and intrinsic properties of RF mounted interband cascade laser," Appl. Phys. Lett. **119**, 171107 (2021).
[32]A. Soibel, M. Wright, W. Farr, S. Keo, C. Hill, R. Q. Yang, and H. Liu, "High-speed operation of interband cascade lasers," Electron. Lett. **45**, 264–265 (2009).
[33]R. Q. Yang, Z. Tian, Z. Cai, J. Klem, M. B. Johnson, and H. Liu, "Interband-cascade infrared photodetectors with superlattice absorbers," J. Appl. Phys. **107**, 054514 (2010).
[34]L. M. Krüger, J. Hillbrand, J. Heidrich, M. Beiser, R. Weih, J. Koeth, C. R. Phillips, B. Schwarz, G. Strasser, and U. Keller, "High-speed interband cascade infrared photodetectors: Photo-response saturation by a femtosecond oscillator," Opt. Express **29**, 14087–14100 (2021).
[35]P. Didier, H. Knötig, O. Spitz, L. Cerutti, A. Lardschneider, E. Awwad, D. Diaz-Thomas, A. Baranov, R. Weih, J. Koeth *et al.*, "Interband cascade technology for energy-efficient mid-infrared free-space communication," Photonics Res. **11**, 582–590 (2023).
[36]A. Soibel, M. W. Wright, W. H. Farr, S. A. Keo, C. J. Hill, R. Q. Yang, and H. Liu, "Midinfrared interband cascade laser for free space optical communication," IEEE Photonics Technol. Lett. **22**, 121–123 (2010).
[37]M. Nedeljkovic, C. G. Littlejohns, A. Z. Khokhar, M. Banakar, W. Cao, J. S. Penades, D. T. Tran, F. Y. Gardes, D. J. Thomson, G. T. Reed *et al.*, "Silicon-on-insulator free-carrier injection modulators for the mid-infrared," Opt. Lett. **44**, 915–918 (2019).
[38]L. Huang, B. Dong, Z. G. Yu, J. Zhou, Y. Ma, Y.-W. Zhang, C. Lee, and K.-W. Ang, "Mid-infrared modulators integrating silicon and black phosphorus photonics," Mater. Today Adv. **12**, 100170 (2021).
[39]M. R. Clay and A. P. Lenham, "Transmission of electromagnetic radiation in fogs in the 0.53–10.1-μm wavelength range," Appl. Opt. **20**, 3831_1 (1981).
[40]N. S. Kopeika, "General wavelength dependence of imaging through the atmosphere," Appl. Opt. **20**, 1532–1536 (1981).
[41]J. Gong, R. Q. Yang, Z. Wang, and J.-J. He, "Single-mode tunable interband cascade laser emitting at 3.4 μm with a wide tuning range over 100 nm," IEEE Photonics Technol. Lett. **35**, 309–312 (2023).
[42]J. A. M. Fordyce, D. A. Diaz-Thomas, L. O'Faolain, A. N. Baranov, T. Piwonski, and L. Cerutti, "Single-mode interband cascade laser with a slotted waveguide," Appl. Phys. Lett. **121**, 211102 (2022).
[43]K. Petermann, *Laser Diode Modulation and Noise* (Springer Science & Business Media, 2012), Vol. 3.
[44]M. Rio Calvo, J.-B. Rodriguez, C. Cornet, L. Cerutti, M. Ramonda, A. Trampert, G. Patriarche, and E. Tournié, "Crystal phase control during epitaxial hybridization of III-V semiconductors with silicon," Adv. Electron. Mater. **8**, 2100777 (2022).
[45]D. A. Díaz-Thomas, O. Stepanenko, M. Bahriz, S. Calvez, E. Tournié, A. N. Baranov, G. Almuneau, and L. Cerutti, "Interband cascade lasers with AlGaAsSb cladding layers emitting at 3.3 μm," Opt. Express **27**, 31425–31434 (2019).
[46]J. Duan, H. Huang, B. Dong, D. Jung, J. C. Norman, J. E. Bowers, and F. Grillot, "1.3-μm reflection insensitive InAs/GaAs quantum dot lasers directly grown on silicon," IEEE Photonics Technol. Lett. **31**, 345–348 (2019).
[47]Z.-F. Fan, Y. Deng, C. Ning, S.-M. Liu, and C. Wang, "Differential gain and gain compression of an overdamped interband cascade laser," Appl. Phys. Lett. **119**, 081101 (2021).
[48]E. Rodriguez, A. Mottaghizadeh, D. Gacemi, D. Palaferri, Z. Asghari, M. Jeannin, A. Vasanelli, A. Bigioli, Y. Todorov, M. Beck *et al.*, "Room-temperature, wide-band, quantum well infrared photodetector for microwave optical links at 4.9 μm wavelength," ACS Photonics **5**, 3689–3694 (2018).
[49]J. Hillbrand, L. Matthieu Krüger, S. Dal Cin, H. Knötig, J. Heidrich, A. Maxwell Andrews, G. Strasser, U. Keller, and B. Schwarz, "High-speed quantum cascade detector characterized with a mid-infrared femtosecond oscillator," Opt. Express **29**, 5774–5781 (2021).
[50]J. Huang, Z. Shen, Z. Wang, Z. Zhou, Z. Wang, B. Peng, W. Liu, Y. Chen, and B. Chen, "High-speed mid-wave infrared uni-traveling carrier photodetector based on InAs/InAsSb type-II superlattice," IEEE Electron Device Lett. **43**, 745–748 (2022).
[51]S. Zhao and F. Grillot, "Stochastic model of sub-poissonian quantum light in an interband cascade laser," Phys. Rev. Appl. **18**, 064027 (2022).
[52]Y. Deng, Z.-F. Fan, B.-B. Zhao, X.-G. Wang, S. Zhao, J. Wu, F. Grillot, and C. Wang, "Mid-infrared hyperchaos of interband cascade lasers," Light: Sci. Appl. **11**, 7 (2022).
[53]HgCdTe (MCT) Detection Module UHSM-I-10.6, https://vigophotonics.com/product/uhsm-i-10-6/, 2023.